Dalton Transactions

RSC Publishing

PAPER

View Article Online
View Journal | View Issue

Cite this: *Dalton Trans.*, 2013, **42**, 8761

High-throughput microwave-assisted discovery of new metal phosphonates†

Mark Feyand,[a] Christopher F. Seidler,[b] Carsten Deiter,[c] Andre Rothkirch,[c] Alexandra Lieb,[d] Michael Wark[b] and Norbert Stock*[a]

Received 13th February 2013,
Accepted 12th April 2013

DOI: 10.1039/c3dt50413a

www.rsc.org/dalton

A systematic study was carried out to investigate the influence of linker geometry, metal ionic radius as well as the nature of the counter ions on the structure formation of metal tetraphosphonates. Two tetraphosphonic acids *p*- and *m*-$(H_2O_3PCH_2)_2N\text{-}CH_2\text{-}C_6H_4\text{-}CH_2\text{-}N(CH_2PO_3H_2)_2$, six metal ions ($Ca^{2+}$, Mn^{2+}, Co^{2+}, Ni^{2+}, Zn^{2+}, and Cd^{2+}) and two different counter ions (Cl^- and NO_3^-) were employed using high throughput methods. Microwave (MW)-assisted heating led to the discovery of ten new metal-phosphonates which crystallize in three different crystal structures. The combination of direct methods and force field calculations allowed us to establish the crystal structures. The counter ion and the ionic radii of the metal ions have a profound influence on the crystallinity and the formed crystal structure. All compounds were characterized in detail by thermogravimetric analyses, IR spectroscopy and magnetic susceptibility measurements. The proton conductivity of two selected compounds is also reported.

Introduction

Metal phosphonates are the focus of recent research activities due to their interesting properties such as magnetism, porosity,[1,2] luminescence[3] or catalysis.[4] Metal phosphonates show a large structural variety depending on the linker molecule or the incorporated metal ion. The properties may change drastically upon variation of the constituents. The inorganic building units observed in metal phosphonates range from isolated clusters[5] to chains[2,6–8] or layers.[8–10]

Suitable methods to synthesize metal phosphonates are solvothermal reactions. Recently, microwave assisted heating was applied to synthesize new metal phosphonates.[7,11,12] Microwave (MW) assisted reactions have proven to lead to higher purities, high yields and much shorter reaction times.[13] However, the sealed reaction conditions make obtaining information about crystallization difficult. In addition, the outcome of such reactions, *i.e.* the product formation, is not predictable and large variable parameters such as temperature, pH or molar ratio of reactants have to be studied exploratively. High-throughput (HT) methods provide a combinatorial and more systematic approach.[14,15] They allow researchers to investigate efficiently and in a fast manner important reaction parameters such as the reaction temperature,[14,16] the concentration of reactants,[17] ionic radii,[18] the pH,[10,16,17] or the length of the organic moiety.[10] Recently HT MW assisted reactions were employed to establish the fields of formation of new metal–organic framework compounds. However, these methods have never been employed in metal phosphonate chemistry before.[19]

We are interested in the synthesis of new metal phosphonates and for the present study we have chosen the tetraphosphonic acids *p*- and *m*-$(H_2O_3PCH_2)_2N\text{-}CH_2\text{-}C_6H_4\text{-}CH_2\text{-}N(CH_2PO_3H_2)_2$. They have previously been shown to lead to three new compounds containing Ca^{2+} and Cu^{2+} ions.[20,21]

Here we present the results of the systematic HT investigation of the synthesis of metal tetraphosphonates using MW-assisted heating and varying the linker geometry as well as the metal and counter ion. In addition, the crystal structures are determined from X-ray powder diffraction data and the detailed characterisation of the products is shown.

Experimental section

Materials and methods

All starting materials were obtained from Aldrich or ABCR and were used without further purification. The two tetraphosphonic acids were synthesized using a slightly modified Mannich-type procedure.[22] XRPD measurements were carried out on a

[a]*Institut für Anorganische Chemie, Christian-Albrechts-Universität, Max-Eyth Straße 2, D 24118 Kiel, Germany. E-mail: stock@ac.uni-kiel.de*
[b]*Lehrstuhl für Technische Chemie, Ruhr-Universität Bochum, Universitätsstr. 150, D44801 Bochum, Germany*
[c]*HASYLAB, DESY Hamburg, Notkestraße 85, 22607 Hamburg, Germany*
[d]*Institut für Chemie, Otto-von-Guericke-Universität, Universitätsplatz 2, 39106 Magdeburg, Germany*

†Electronic supplementary information (ESI) available: Assymetric units, details about the structure determination, thermogravimetric measurements. See DOI: 10.1039/c3dt50413a

Stoe Stadi P diffractometer in transmission geometry with Cu-$K_{\alpha1}$ radiation, equipped with an image plate detector system or a linear PSD detector system for high resolution data. The MIR spectra were recorded on a Bruker ALPHA-P FT-IR spectrometer in the spectral range 4000–400 cm^{-1}. For the thermogravimetric analyses under air a NETZSCH STA 409 CD analyzer was used with a heating rate of 4 K min^{-1} and an air flow rate of 75 mL min^{-1}. High resolution powder XRD patterns were measured at beamline G3 (light source DORIS)[23] and beamline P08 (light source PETRA)[24] both at HASYLAB, DESY. Scaled up syntheses under conventional heating were carried out under solvothermal conditions using DURAN culture tubes D50 GL 14 M.KAP, SCHOTT. An Anton Paar Synthos 3000 microwave reactor was used for the high-throughput syntheses. Temperature dependent X-ray diffraction patterns were recorded on a Panalytical Empyrean diffractometer equipped with a PIXcell detector using a MRI TC radiation chamber with a Pt heater and Al_2O_3 crucibles.

Synthesis of *p*-$(H_2O_3PCH_2)_2NCH_2$-C_6H_4-$CH_2N(CH_2PO_3H_2)_2$ (*p*-H_8L). 5.00 g (36.7 mmol) *p*-xylenediamine and 12.0 g (147 mmol) phosphorous acid were added to 60 mL half concentrated hydrochloric acid.[22] The mixture was heated to reflux and 13 mL (161 mmol) 37% formalin solution was slowly added. The reaction was then heated for 14 h and cooled to room temperature. The white precipitate was filtered and washed with deionized water. The product was identified as *p*-H8L by ^{1}H and ^{31}P-NMR spectroscopy (yield 45.17 g 60% based on *p*-xylenediamine) (see the ESI†).

Synthesis of *m*-$(H_2O_3PCH_2)_2NCH_2$-C_6H_4-$CH_2N(CH_2PO_3H_2)_2$ (*m*-H_8L). 10.00 g (73.4 mmol) *m*-xylenediamine and 24.0 g (294 mmol) phosphorous acid were added to 60 mL half concentrated hydrochloric acid.[22] The mixture was heated to reflux and 26 mL (322 mmol) 37% formalin solution were slowly added. The reaction was then heated for 14 h and cooled to room temperature. The white precipitate was filtered and washed with deionized water. The product was identified as *m*-H_8L by ^{1}H and ^{31}P-NMR spectroscopy (yield 67.76 g 45% based on *m*-xylenediamine) (see the ESI†).

HT microwave assisted reactions. The HT syntheses were carried out in 4 mL microwave glass vials in a 24 reactor setup using an Aton Parr HT reactor system. The reactions were carried out at 150 °C for 5 h using a power of 400 W. The molar ratio $H_8L : M^{2+}$ was kept at 1 : 1 and the concentration was fixed by using 25 mg of H_8L per reaction. To investigate the influence of the linker geometry 12 reactions per linker were carried out. To investigate different metal ion radii we studied Mn^{2+}, Ca^{2+}, Co^{2+}, Ni^{2+}, Zn^{2+} and Cd^{2+} using Cl^- and NO_3^- as counter ions. The obtained products were identified by X-ray powder diffraction. The results of the high-throughput investigation are summarized in Fig. 2. The exact reaction conditions are given in the ESI (Table S1†).

Scale-up synthesis of Cd[*p*-$(HO_3PCH_2)_2N(H)$-CH_2-C_6H_4-CH_2-$N(H)(CH_2PO_3H)_2$] (1). 40 mg *p*-H_8L (78 mmol), 117 μL (234 mmol) of a 2 M $CdCl_2$ solution and 3 mL deionized water were mixed in DURAN culture tubes, sealed and heated up to 150 °C for 12 h. The reaction mixture was filtered and washed with water. Using pH paper pH = 2 was determined for the initial and final reaction solutions. The yield was 33 mg, 68% based on *p*-H_8L.

Scale-up syntheses of M[*p*-$(HO_3PCH_2)_2N(H)$-CH_2-C_6H_4-CH_2-$N(H)(CH_2PO_3H)_2(H_2O)$] (M = Mn, Co, Ni, Zn) (2). 40 mg *p*-H_8L (78 mmol), 39 μL (78 mmol) of a 2 M $M(NO_3)_2$ solution and 3 mL deionized water were mixed in DURAN culture tubes, sealed and heated up to 150 °C for 12 h. The reaction mixture was filtered and washed with water. Using pH paper pH = 2 was determined for the initial and final reaction solution. The yields were 34, 13, 23, 26 mg, 70, 25, 45, 50% based on *p*-H_8L, for M = Mn, Co, Ni, Zn, respectively.

Scale-up syntheses of M[*m*-$(HO_3PCH_2)_2N(H)$-CH_2-C_6H_4-CH_2-$N(H)(CH_2PO_3H)_2]\cdot H_2O$ (M = Ca, Mn, Co, Ni, Zn) (3). 40 mg *m*-H_8L (78 mmol), 39 μL (78 mmol) of a 2 M MCl_2 solution, 20 μL (39 mmol) of a 2 M NaOH solution and 3 mL deionized water were mixed in DURAN culture tubes, sealed and heated up to 150 °C for 12 h. The reaction mixture was filtered and washed with water. Using pH paper pH = 2 was determined for the initial and final reaction solutions. The yields were 38, 26, 40, 20, 21 mg (75, 50, 85, 42, 42% based on *m*-H_8L), for M = Ca, Mn, Co, Ni, Zn, respectively.

Crystal structure determination

All compounds were obtained as microcrystalline powders. Thus, the structures had to be determined from X-ray powder diffraction data. The important crystallographic parameters are given in Table 1.

Crystal structure determination of compound 1. High resolution XRPD data of compound **1** (Cd) were collected at beamline G3, HASYLAB, DESY, Hamburg using a wavelength of 1.54296(2) Å selected by a double silicon single crystal monochromator and determined with a LaB_6 standard. The diffracted beam was detected by a scintillation counter mounted behind a soller slit system. The sample was measured in a capillary (0.7 mm diameter). The powder pattern was successfully indexed using Topas Academic and the possible space group $P2_1/a$ was suggested.[11] The crystal structure was solved in $P2_1/a$ using direct methods implemented in EXPO2009. The heavy atom positions and the phosphonate groups could be located directly from the Fourier map. The structure model was completed using Materials Studio 5.3 applying force field calculations.[25] A universal force field was used as implemented in Materials Studio. The obtained model was further refined by Rietveld methods in the 2θ range of 9 to 80° using Topas Academic. The final Rietveld refinement included six background points, three Thompson–Cox–Hastings profile parameters, four lattice parameters, one scaling factor, a simple axial model, a fourth order spherical harmonics series, 45 atomic coordinates and three temperature factors (Cd, P, and C/N/O). The P–O and P–C distances were soft restrained. The final Rietveld plot is given in Fig. 3.

Crystal structure determination of compound 2. A high resolution XRPD pattern of compound **2** (Zn) was recorded at beamline P08, PETRA, DESY, Hamburg with a wavelength of 0.824516 Å. The powder pattern was successfully indexed using

Table 1 Crystallographic data of compounds **1**, **2** and **3** (SH = spherical harmonics series)

	Compound **1**	Compound **2**	Compound **3**
Formula sum	$C_{10}H_{18}N_2CdO_{12}P_4$	$C_{10}H_{20}N_2ZnO_{13}P_4$	$C_{10}H_{20}N_2NiO_{13}P_4$
Radiation source	Synchrotron	Synchrotron	Laboratory
Wavelengths/Å	1.54296	0.824516	$CuK\alpha_1$
a/Å	12.1198(4)	10.5960(3)	22.2633(4)
b/Å	15.1091(4)	7.5569(2)	8.5904(2)
c/Å	5.5632(1)	6.9120(2)	9.8834(2)
α/°	90	106.42(2)	90
β/°	97.28(2)	98.50(3)	90
γ/°	90	86.79(1)	90
Space group	$P2_1/a$	$P\bar{1}$	*Pmcn*
R_{wp}	2.80	3.60	5.77
R_{Bragg} (without SH)	1.03(3.25)	0.79(4.25)	1.86(8.74)
GoF	1.42	1.97	1.81
Number of restraints	6	8	10
Number of parameters	80	85	78
Volume/Å^3	1010.62(5)	524.99(4)	1890.22(6)
Z	2	1	4

Topas Academic. Due to the small cell volume of 525(1) Å^3 only one twofold deprotonated linker ion and one Zn^{2+} ion are present in the unit cell. A structure model was derived in the space group $P\bar{1}$ by molecular modeling using Materials Studio 5.3. Details are given in the ESI (Fig. S3†). The starting model was refined by Rietveld methods in the range of 4–40° 2*θ* using Topas Academic. The final Rietveld refinement included six background points, three Thompson–Cox–Hastings profile parameters, six lattice parameters, one scaling factor, a simple axial model, a fourth order spherical harmonics series, 48 atomic coordinates and three (Zn, P, and C/N) temperature factors. The P–O and P–C distances were soft restrained. The final Rietveld plot is given in Fig. 5.

Crystal structure determination of compound 3. The powder pattern of **3** (Ni) was collected on a Stoe Stadi P diffractometer equipped with a linear PSD detector. The structure was solved using direct methods implemented in EXPO2009. The inorganic building unit was directly located from the Fourier map and completed by force field calculations using Materials Studio 5.3. The structural model was refined by Rietveld methods in the range of 9 to 75° 2*θ* using Topas Academic. The final Rietveld refinement subsumed six background points, three Thompson–Cox–Hastings profile parameters, four lattice parameters, one scaling factor, a simple axial model, a fourth order spherical harmonics series, 45 atomic coordinates and three (Ni, P, and C/N/O) temperature factors. The P–O, P–C and some C–C distances were soft restrained. The final Rietveld plot is given in Fig. 7.

Proton conductivity

Proton conductivity was determined by impedance spectroscopy (IS).[26,27] An oscillating voltage of 100 mV was applied over a frequency range from 1 to 10^6 Hz using a Zahner Zennium electrochemical workstation. The powder samples were pressed into small pellets (diameter 8 mm, thickness 0.5–1.5 mm) and incorporated into a stack comprising the sample sandwiched between two graphitic slices. The stack was placed in a PTFE sample holder, and two sintered metal electrodes were used to make electrical contact with the stack. The sample holder was placed in a gas-tight, temperature-controlled stainless steel chamber with an attached water reservoir.[28] The relative humidity (RH) in the cell was determined by the Clausius–Clapeyron relation and controlled by heating the water reservoir and the cell. Preceding each series of measurements, samples were equilibrated for 24 hours at 313 K and at 50% RH. The sample was equilibrated for 1 hour at the desired temperature and RH before measuring each data point. Each point was measured three times to determine reproducibility.

Results and discussion

To investigate the influence of the linker geometries the two tetraphosphonic acids *p*-$(H_2O_3PCH_2)_2N\text{-}CH_2C_6H_4CH_2\text{-}N(CH_2PO_3H_2)_2$ (*p*-H_8L) and *m*-$(H_2O_3PCH_2)_2N\text{-}CH_2C_6H_4CH_2\text{-}N(CH_2PO_3H_2)_2$ (*m*-H_8L) were synthesized (Fig. 1).

High throughput investigation

The influence of the geometry of tetraphosphonic acid on the formation of metal phosphonates was investigated using high-throughput methods.[15] Thus six different metal ions with ionic radii between 0.74 and 1.14 Å (Mn^{2+}, Ca^{2+}, Co^{2+}, Ni^{2+}, Zn^{2+} and Cd^{2+}) and different counter ions (NO_3^- and Cl^-) were

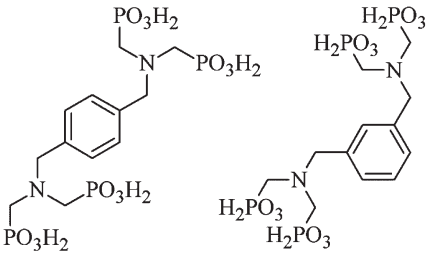

Fig. 1 Linker molecules used in this study. Left: *p*-$(H_2O_3PCH_2)_2N\text{-}CH_2C_6H_4CH_2\text{-}N(CH_2PO_3H_2)_2$ (*p*-H_8L), right: *m*-$(H_2O_3PCH_2)_2N\text{-}CH_2C_6H_4CH_2\text{-}N(CH_2PO_3H_2)_2$ (*m*-H_8L).

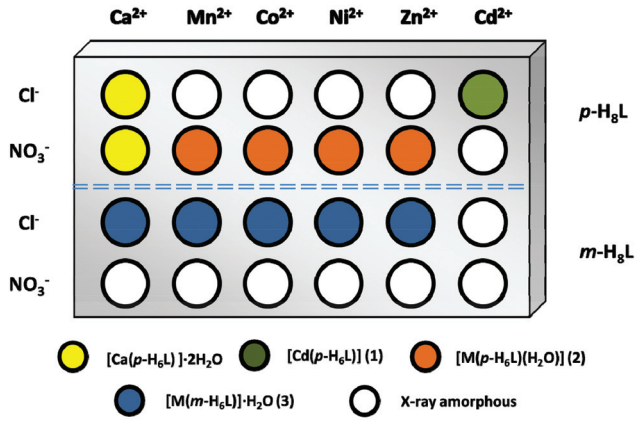

Fig. 2 Results of the high-throughput study. The compound $[Ca(p\text{-}H_6L)]\cdot 2H_2O$ has already been reported before.[21]

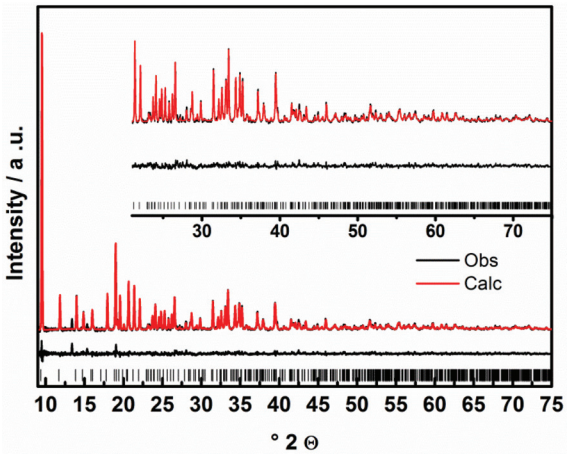

Fig. 3 Final Rietveld plot of **1**. The observed powder pattern is shown in black, the calculated powder pattern as an overlay in red and the difference (observed – calculated) of both is given by the lower black line. The allowed positions of the Bragg peaks are given as ticks. The inset shows the higher 2θ range.

used. 24 reactions were carried out under microwave assisted heating at 150 °C for 5 h and a molar ratio of $H_8L : M^{2+} = 1 : 1$ (details are given in Table S1†). The results of the study are presented in Fig. 2.

Using *p*-H_8L and metal chlorides $CdCl_2$ leads to a highly crystalline compound of composition $[Cd(HO_3PCH_2)_2NH\text{-}CH_2C_6H_4CH_2\text{-}NH(CH_2PO_3H)_2]$ (**1**). The use of metal nitrates instead of metal chlorides leads to the isostructural compounds $[M(HO_3PCH_2)_2NH\text{-}CH_2C_6H_4CH_2\text{-}NH(CH_2PO_3H)_2(H_2O)]$ (**2**) with M = Mn^{2+}, Co^{2+}, Ni^{2+} and Zn^{2+}, respectively. Using Cd^{2+} as the cation, only X-ray amorphous powders were obtained. Both Ca^{2+} salts lead to the literature known compound $[Ca(p\text{-}H_6L)]\cdot 2H_2O$ in much shorter reaction times of 5 h compared to 48 h using conventional heating. In contrast, reactions of *m*-H_8L with metal nitrates lead to X-ray amorphous compounds while reactions with metal chlorides result in crystalline compounds $[M(HO_3PCH_2)_2NH\text{-}CH_2\text{-}C_6H_4\text{-}CH_2\text{-}NH(CH_2PO_3H)_2]\cdot(H_2O)$ (**3**) for M = Mn^{2+}, Ca^{2+}, Co^{2+}, Ni^{2+} and Zn^{2+} and an X-ray amorphous product for M = Cd^{2+}.

Crystal structure of $[Cd(HO_3PCH_2)_2NH\text{-}CH_2C_6H_4CH_2\text{-}NH(CH_2PO_3H)_2]$ (1). Using high resolution powder diffraction data the structure of **1** was determined by a combination of direct methods and molecular modeling. The final results of the structure refinement are given in Fig. 3.

The crystal structure of **1** is shown in Fig. 4 (and S4†). Each Cd^{2+} ion is six-fold coordinated with oxygen. These oxygen atoms derive from six different phosphonate groups. The formed polyhedra are connected by the phosphonate groups to one-dimensional chains along the *c*-axis. These chains are interconnected by the rest of the linker molecules to form a three dimensional network. The non-coordinating phosphonate groups are involved in hydrogen bonds which are shown in the ESI (Fig. S6†).

Crystal structure of $[Zn(HO_3PCH_2)_2NH\text{-}CH_2C_6H_4CH_2\text{-}NH(CH_2PO_3H)_2(H_2O)]$ (2 (Zn)). Taking into account the unit cell dimension, the space group symmetry and the unit cell content a structural model for **2** was derived by molecular modeling. The model was successfully refined using high resolution X-ray diffraction data (Fig. 5). The coordination

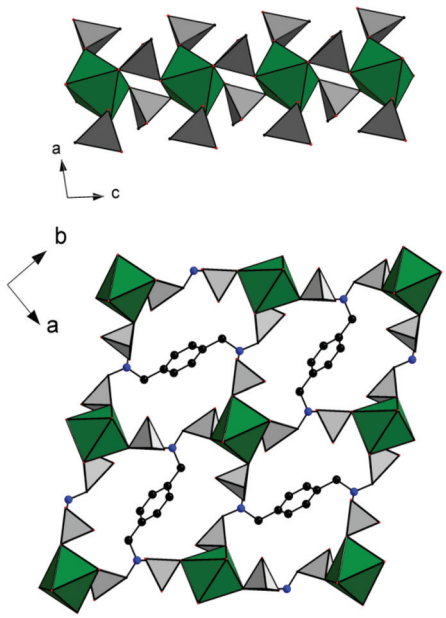

Fig. 4 Crystal structure of compound **1**. Chains of corner-sharing CdO_6 and O_3PC polyhedra along the *c*-axis (top) and their connection to a three-dimensional network (bottom). MO_6 polyhedra are shown in green, O_3PC polyhedra in grey, and nitrogen and carbon atoms in blue and black, respectively.

environment of the Zn^{2+} ions and the interconnection of the metal ions by the linker molecules are shown in Fig. S7,† a section of the crystal structure in Fig. 6. The Zn^{2+} ions are sixfold coordinated by oxygen atoms of four different phosphonate groups and two water molecules. These ZnO_6 polyhedra are connected by the organic linker molecules along [010] to form sheets (Fig. 6, middle), which are connected *via* two different kinds of hydrogen bonds (PO–H···OP and PO–H···OH) as indicated by the donor–acceptor distances (Fig. S8†) between HO_3PC-groups phosphonate dimers.

The allowed positions of the Bragg peaks are given as ticks.

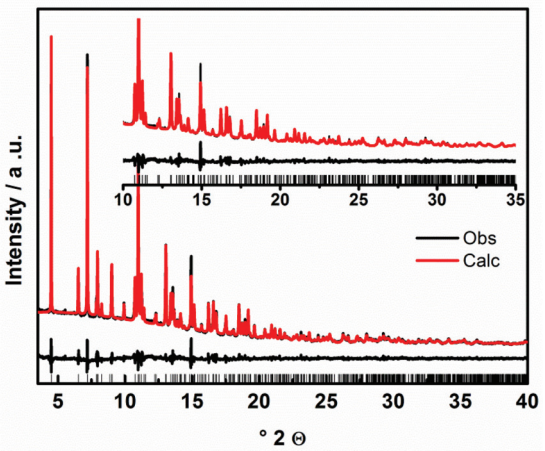

Fig. 5 Final Rietveld plot of **2** (Zn). The observed powder pattern is shown in black, the calculated powder pattern as an overlay in red and the difference (observed – calculated) of both is given by the lower black line. The allowed positions of the Bragg peaks are given as ticks. The inset shows the higher 2θ range.

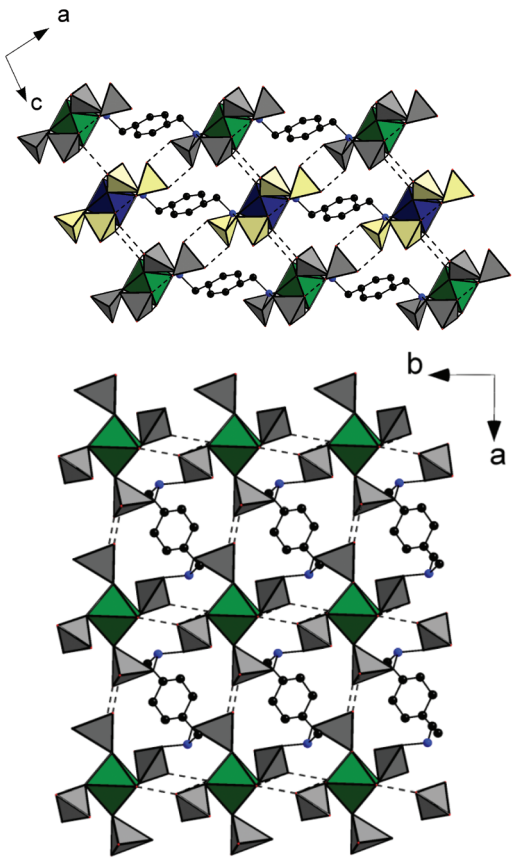

Fig. 6 Crystal structure of compound **2** (Zn). Connection of the Zn^{2+} ions by *p*-H_6L^{2-} ions in the *a*,*b*-plane (bottom) and possible interconnection of the layers by postulated hydrogen bonds (top). MO_6 polyhedra are shown in green, O_3PC polyhedra in grey, and nitrogen and carbon atoms in blue and black, respectively. One layer is shown by blue MO_6 and yellow CPO_3 polyhedra.

Crystal structure of $[Ni(HO_3PCH_2)_2NH\text{-}CH_2C_6H_4CH_2\text{-}NH\text{-}(CH_2PO_3H)_2]\cdot H_2O$ (3 (Ni)). *In house* XRPD data were used for the structure determination of **3** (Ni). Direct methods in combination with difference Fourier calculations and molecular modeling led to a structural model that was successfully refined by Rietveld methods (Fig. 7). The coordination environment of the Ni^{2+} ions and the interconnection of the metal ions by the linker molecules are shown in Fig. S7† and the crystal structure is shown in Fig. 8. Each Ni^{2+} ion is sixfold coordinated by oxygen atoms of six different phosphonate groups and layers in the *b*,*c*-plane are formed. These layers are interconnected to a three dimensional network by the organic linker molecules. Based on P–O···O–P and P–O···OH_2 distances between 2.50(2) and 3.06(2) Å hydrogen bonds can be postulated that further stabilize the structure (Fig. S9†).

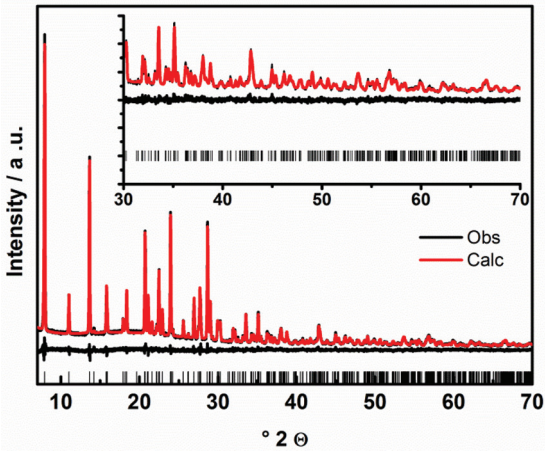

Fig. 7 Final Rietveld plot of **3** (Ni). The observed powder pattern is shown in black, the calculated powder pattern as an overlay in red and the difference (observed – calculated) of both is given by the lower black line. The allowed positions of the Bragg peaks are given as ticks. The inset shows the higher 2θ range.

Structural trends

As a result, from the crystal structures we can conclude that the ionic radius has a crucial influence on the crystal structure formation. Using *p*-H_8L with Ca^{2+} ions with the largest ionic radius (r_{ionic} = 1.14 Å) leads to the literature known compound $[Ca(p\text{-}H_6L)]\cdot 2H_2O$[21] whereas the much smaller ions Mn^{2+}, Ni^{2+}, Co^{2+}, and Zn^{2+} (r_{ionic} = 0.81, 0.79, 0.83, 0.88 Å, respectively) form an isostructural compound. Cd^{2+} ions with an intermediate ionic radius of 1.09 Å crystallizes in a different crystal structure (compound **1**). All structures are pseudopolymorphic with **1** containing no, **2** one and $[Ca(p\text{-}H_6L)]\cdot 2H_2O$ two water molecules per formula unit. Thus, the Cd^{2+} ions in **1** seem to have the right size to allow for the formation of a three dimensional coordination polymer. In contrast, layers are formed which are connected by hydrogen bonds for the structure of compound **2**. This leads to a higher flexibility of the network and can adjust to different ionic radii. In contrast the use of *m*-H_8L leads to one isostructural compound for Mn^{2+}, Ni^{2+}, Co^{2+}, Ca^{2+} and Zn^{2+}.

IR spectroscopy

To learn more about the properties of the compounds we carried out IR spectroscopic and thermogravimetric

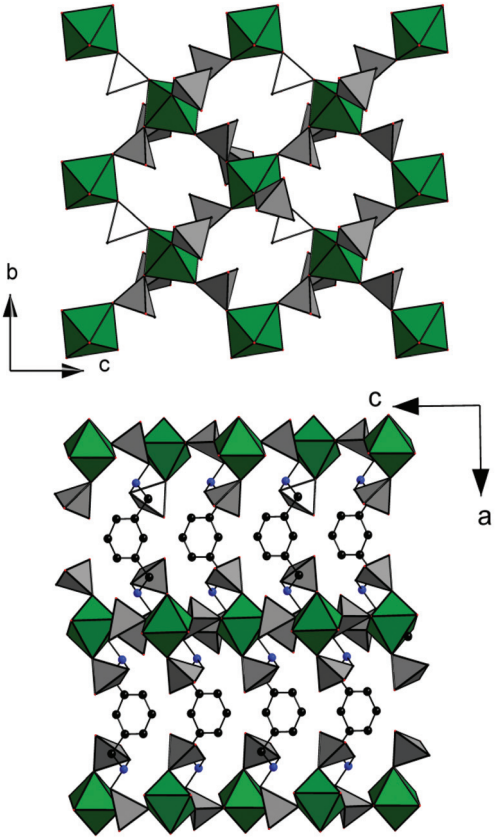

Fig. 8 Crystal structure of **3**. View along the *a*-axis (top) onto the layers and view along the layers connected by the organic linker molecules along the *b*-axis (bottom). Water molecules were omitted for clarity.

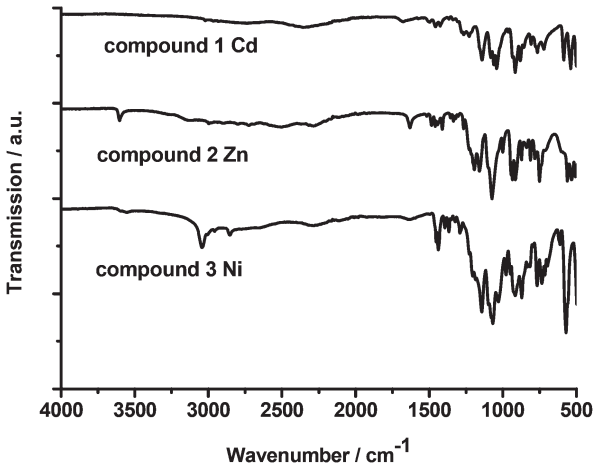

Fig. 9 IR-spectra of compounds **1**, **2** and **3**.

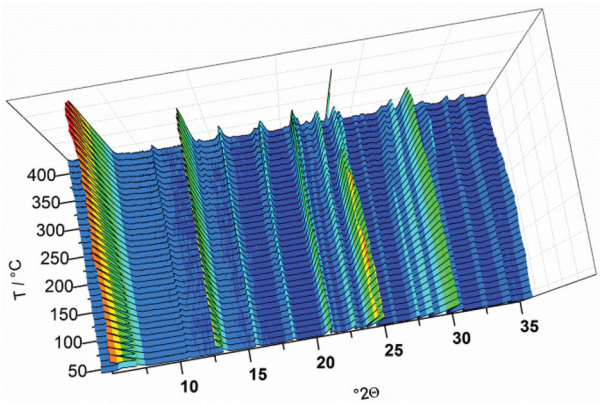

Fig. 10 Results of the temperature dependent XRPD measurements of compound **3** (Ni). The Bragg peak at ~23.2° 2θ is due to the sample holder.

measurements. The IR spectra of compound **1** (Cd), **2** (Zn) and **3** (Ni) are shown in Fig. 9. All other IR spectra are given in the ESI (Fig. S9 and S11†).

All three compounds show a very similar IR-spectrum. In the range between 1250 and 980 cm^{-1} the typical CPO_3-bands are observed. The aromatic and aliphatic C–H stretching vibrations are observed in the region between 3098 and 2970 cm^{-1} and broad P–OH bands can be observed between 2840 and 2200 cm^{-1}. In accordance with the crystallographic data a broad band around 3600 cm^{-1} from the coordinated and uncoordinated water molecules of compound **2** and **3** is present.

Thermal stability

The thermal stability was investigated by thermogravimetric analyses (TG). The results of all TG measurements are given in the ESI (Fig. S12 and S13†). All compounds show different thermal stabilities. Compound **1** (Cd) is stable up to 300 °C and decomposes in a multiple step decomposition. As expected, compounds **2** (Zn) and **3** (Ni) show in addition to the decomposition in the range between 100 and 200 °C one step of weight loss which is due to the coordinated and uncoordinated water molecules. The removal of the uncoordinated water molecule in **3** (Ni) was further investigated by temperature dependent XRPD in the range of 40–400 °C (Fig. 10).

The sample is stable up to at least 400 °C and shows slight shifts of the Bragg peaks and changes in the intensity above 200 °C. This can be explained by the loss of the water molecule. The lattice parameters of each pattern were extracted using parametric Pawley refinement methods as implemented in Topas academic[11] using the program Powder3D parametric.[29] The results are shown in Fig. 11. Up to 200 °C all lattice parameters and the cell volume are slightly increasing as expected due to the thermal expansion of the lattice. Above 200 °C the lattice parameters *a*- and *c*-axis as well as the cell volume are rapidly decreasing due to the loss of the water molecule while the *b*-axis length is further increasing. The cell volume is decreasing above 200 °C.

These lattice parameter changes with temperature can be explained by inspecting the crystal structure of **3** (Ni). Along [100] and [001] PO···OP and PO···Ow···OP hydrogen bonds are observed (Fig. S9†). Removal of the water molecule (Ow) therefore results in a decrease of the *a*- and *c*-parameter. In contrast,

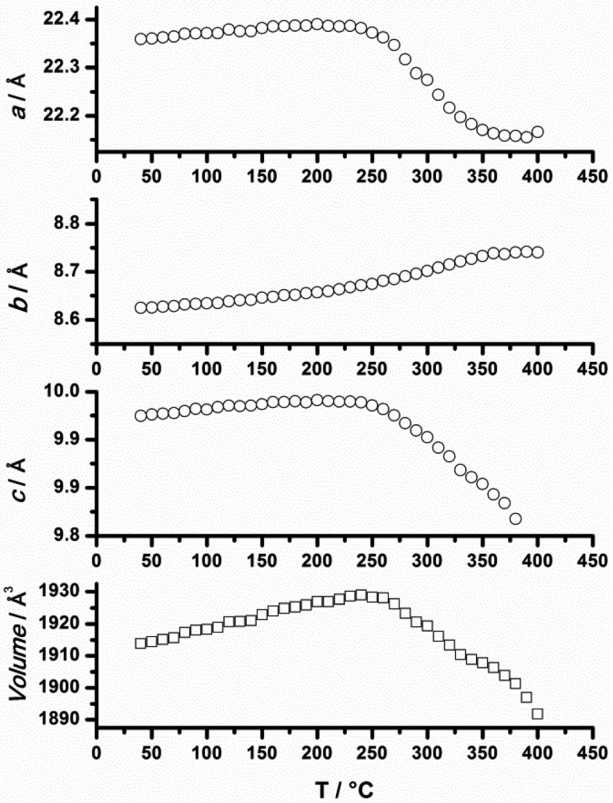

Fig. 11 Evolution of lattice parameters of compound **2**. Parameters were obtained by parametric Pawley refinement.

along [010] no hydrogen bonds are observed which is reflected in the increase of the *b*-parameter with temperature.

Magnetic properties of 3 (Mn, Co and Ni)

Since compounds **2** (Mn, Co, Ni) decompose upon evacuation of the samples, only the compounds **3** (Mn, Co, Ni) were investigated for their magnetic properties. In that case, temperature and field dependent magnetic susceptibility measurements were performed.

Magnetic properties of $[Mn(HO_3PCH_2)_2NH\text{-}CH_2C_6H_4CH_2\text{-}NH(CH_2PO_3H)_2]\cdot H_2O$. The temperature dependent magnetic susceptibility was measured in the temperature range of 300–2 K applying an external field of 0.1 T. The χ *vs.* T and $1/\chi$ *vs.* T plots for **3** (Mn) are given in Fig. 12. The compound shows a typical Curie–Weiss behavior in the temperature range of 300–9 K. Below this temperature regime the compound shows antiferromagnetic coupling. A least-square fit using the Curie–Weiss law leads to C = 4.48 K cm^3 mol^{-1}, and θ = −8.15 K, both in agreement with antiferromagnetic coupling. We observe a μ_{eff} of 5.98μ_b which is in good agreement with the theoretical value of 5.92μ_b for a high spin Mn^{2+} ion.

Magnetic properties of $[Ni(HO_3PCH_2)_2NH\text{-}CH_2C_6H_4CH_2\text{-}NH(CH_2PO_3H)_2]\cdot H_2O$. The results of the temperature dependent magnetic susceptibility measurement of compound **3** (Ni) are shown in Fig. 13. The measurement was carried out in the temperature range of 300–2 K. The compound shows a

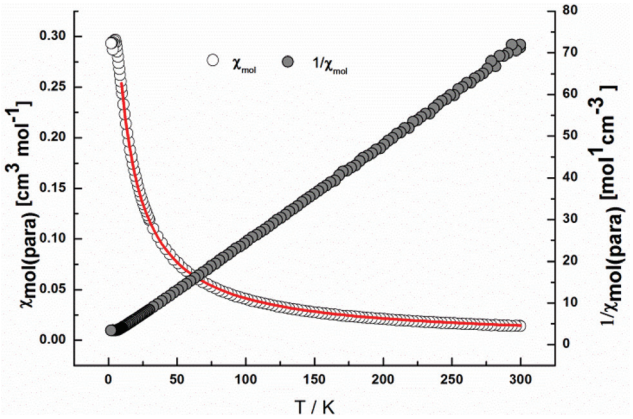

Fig. 12 Temperature dependent magnetic susceptibility of $[Mn(HO_3PCH_2)_2NH\text{-}CH_2C_6H_4CH_2\text{-}NH(CH_2PO_3H)_2]\cdot(H_2O)$. The molar magnetic susceptibility is shown as white dots, the red line shows the Curie–Weiss fit and the reciprocal magnetic susceptibility is shown as grey dots.

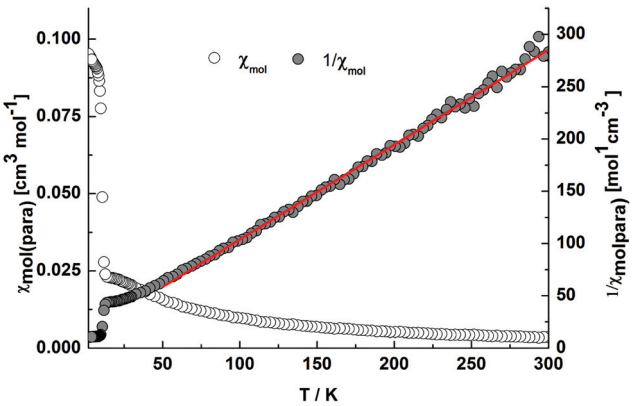

Fig. 13 Temperature dependent magnetic susceptibility of $[Ni(HO_3PCH_2)_2NH\text{-}CH_2C_6H_4CH_2\text{-}NH(CH_2PO_3H)_2]\cdot H_2O$. The molar magnetic susceptibility is shown as white dots, the reciprocal magnetic susceptibility is shown as grey dots and the red line shows the linear fit of $1/\chi$ *vs.* T.

typical paramagnetic behavior between 300 and 50 K. Below 13.3 K ferromagnetic coupling is observed. Linear regression of the $1/\chi$ *vs.* T plot leads to values of C = 1.10 K cm^3 mol^{-1} and θ = 13.26 K which indicates ferromagnetic coupling. We observe a μ_{eff} of 2.98μ_b which is in good agreement with the expected value for a Ni^{2+} ion of 2.83μ_b. To learn more about the ferromagnetic coupling a field dependent measurement at 4.2 K in the range of −9 T to 9 T was carried out. The obtained hysteresis loop is shown in Fig. 14. From that loop a magnetic reminiscence of $+M_r = 0.013N\beta$ mol^{-1}, $-M_r = -0.013N\beta$ mol^{-1} and H_c = 0.160 T, $-H_c$ = −0.159 T was determined.

Magnetic properties of $[Co(HO_3PCH_2)_2NH\text{-}CH_2C_6H_4CH_2\text{-}NH(CH_2PO_3H)_2]\cdot H_2O$. The temperature dependent magnetic susceptibility of compound **3** (Co) is shown in Fig. 15. The measurements were carried out in the temperature range of 300–2 K with zero field cooling (ZFC). The magnetic behavior is similar to the canted antiferromagnetic coupling observed in $Co[HO_2C(CH_2)_3NH(CH_2PO_3H)_2]_2$ which is built up

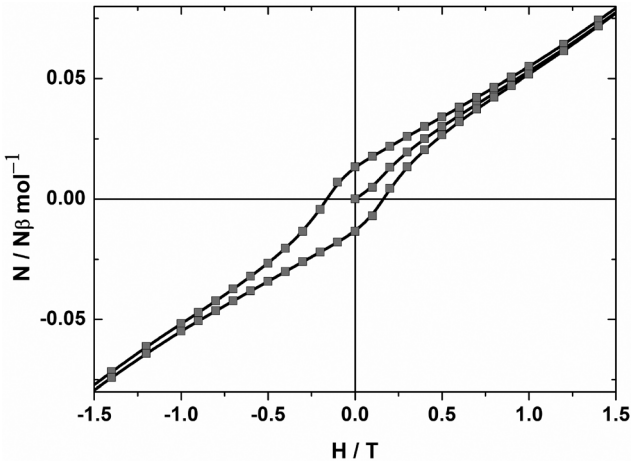

Fig. 14 Field dependent magnetic susceptibility measurement of **3** (Ni) at 4.2 K.

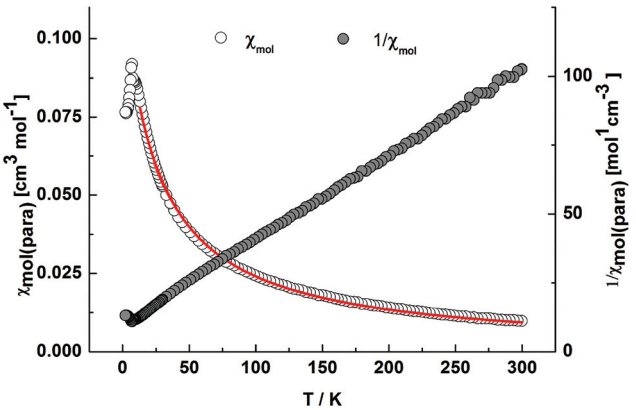

Fig. 15 Temperature dependent magnetic susceptibility of $[Co(HO_3PCH_2)_2NH\text{-}CH_2C_6H_4CH_2\text{-}NH(CH_2PO_3H)_2]\cdot H_2O$. The molar magnetic susceptibility is shown as white dots, the red line shows the Curie–Weiss fit and the reciprocal magnetic susceptibility is shown as grey dots.

from the same inorganic layered motif.[30] The temperature dependent measurement shows paramagnetic behavior in the temperature range between 300–13 K and antiferromagnetic coupling below 13 K. Nevertheless the susceptibility splits upon ZFC. A fit of the χ *vs.* T curve with the Curie–Weiss law leads to C = 3.03 K cm^3 mol^{-1} and θ = −29.50 K. We observe a μ_{eff} of 5.02μ_b which is much higher than the expected spin-only value of μ_{eff} = 3.87μ_b. However, this is in good agreement with the literature value of the canted antiferromagnet (μ_{eff} = 5.23μ_b) which can be explained by the spin orbital interactions of the Co^{2+} ions.

To understand the magnetic behaviour a field dependent initial curve and AC measurements were carried out (Fig. 16). The initial curve shows no step in the range of 0 to 9 T. Thus, a metamagnet can be excluded. The AC measurements show no shift in the maximum susceptibility. These results exclude the presence of spin glass or a ferromagnet. Thus, all results are in agreement with the presence of a canted antiferromagnet.

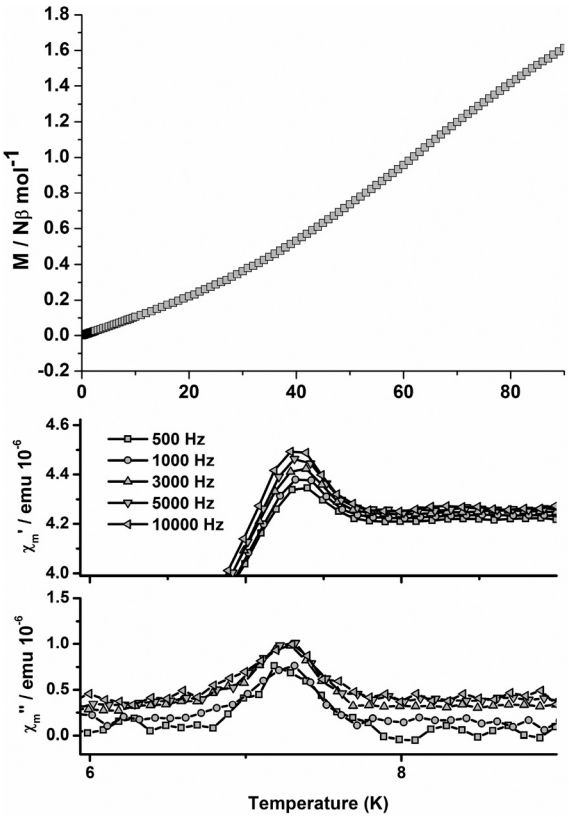

Fig. 16 Initial curve of the field dependent measurement of **3** (Co) at 4.2 K (top) and AC measurements of the susceptibility (bottom).

Proton conductivity

The compounds **2** (Zn) and **3** (Mn) were investigated for their proton conductivity properties because of their expected low toxicity and good crystallinity. While in **2** (Zn) one water molecule per formula unit is coordinated to the zinc ion in **3** (Mn) it is close to the $-PO_3H^-$ groups and is involved in hydrogen bonding. The proton conductivity was determined using eqn (1).[26]

$$\sigma = \frac{1L}{RA} \quad (1)$$

where R: ohmic resistance, σ: proton conductivity, L: sample thickness, A: sample cross-section area.

The ohmic resistance was taken from the Bode phase plot of the impedance, which shows the impedance phase shift *versus* frequency. The impedance corresponding to the phase shift closest to zero is approximately equal to the ohmic resistance of the sample.[26,27] Each impedance value was measured three times, and the arithmetic mean was used in the analyses.

Both metal phosphonates exhibit proton conductivity (Fig. 17); however, the proton conductivity at 413 K and 100% RH of compound **3** (Mn) (1.53 × 10^{-3} S cm^{-1}) is not only 35 times higher than that of **2** (Zn) (4.26 × 10^{-5} S cm^{-1}), but also much more reproducible (rep.). The proton conductivity of **3** (Mn) is in the same order of magnitude as observed for the compound $[Mg((HO_3PCH_2)_2NH\text{-}C_8H_{16}\text{-}NH(CH_2PO_3H)_2]\cdot 6H_2O$, which exhibits a value of 1.6 × 10^{-3} S cm^{-1} at 298 K.[31] As

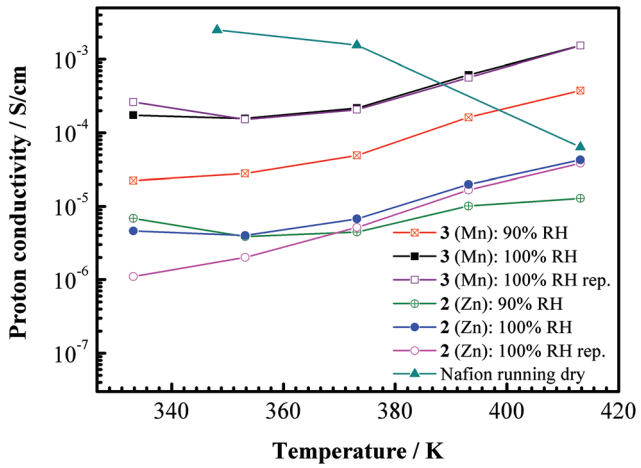

Fig. 17 Proton conductivity of the two phosphonates ([$Zn(HO_3PCH_2)_2NH$-$CH_2C_6H_4CH_2$-$NH(CH_2PO_3H)_2(H_2O)$] – **2** (Zn) and [$Mn(HO_3PCH_2)_2NH$-$CH_2C_6H_4$-CH_2-$NH(CH_2PO_3H)_2$]·H_2O – **3** (Mn)) at different temperatures and relative humidities (90% RH and 100% RH), compared to the polymer Nafion® at 100% RH.[32]

expected, relative humidity has a strong influence on the proton conductivity of the investigated phosphonates: for example, a 10% decrease of RH at 413 K results in a 5-fold decrease in the proton conductivity of **3** (Mn).

At temperatures above 393 K, the proton conductivity of **3** (Mn) exceeds that of Nafion®, which is the most widely used polymer as membrane in Proton Exchange Membrane Fuel Cells (PEMFC). In contrast to Nafion® for which the loss in conductivity at these high temperatures is well-documented due to dehydration of the membrane,[33] the metal ions and the phosphonate groups seem to interact well enough with the water molecules under the measurement conditions to keep water molecules in the structures.

Thus, the metal phosphonates are comparable to oxide nanoparticles or functionalized ordered mesoporous oxides being widely discussed as additives for PEMFCs in order to avoid the shortcomings of Nafion® at high temperatures and low relative humidities.[34] Since especially sulfonic acid functionalized variants of MCM-41, obtained by co-condensation, exhibit very high proton conductivities up to 0.2 S cm^{-1},[32] new metal sulfonates with defined porosity might be an even more prospective class of materials.

XRD measurements reveal that during the impedance spectroscopy measurement (Fig. S14 and S15†), **2** (Zn) is in part transformed into a new crystalline product whose structure is unknown. The structural change causes conductivity losses and corresponding irreproducibility observed in the **2** (Zn) impedance spectra. In contrast, the second metal phosphonate, **3** (Mn), shows no significant changes in the XRD pattern after IS, and thus features reproducible impedance data.

Conclusion

High-throughput methods employing microwave-assisted heating were shown to be an excellent tool for the rapid discovery of metal phosphonates. Although the counter ions of the metal salts employed are not incorporated into the structure, they have a distinct influence on the crystallinity of the resulting compound. Thus the systematic investigation using different counter ions of metal salts is important.

Since all compounds in this study are obtained as microcrystalline powders, the structure determination had to be carried out from X-ray powder diffraction data. Here, the combined approach of direct methods and force field calculations to establish a structural model has proven to be very valuable. Subsequent Rietveld refinements could be carried out to obtain the crystal structures. Here the results observed for reactions with *p*-H_8L are especially interesting. Depending on the ionic radii of the metal ions three different crystal structures are formed. This suggests that systematic studies on the influence of ionic radii are important for the discovery of new structures.

Finally the isostructural compounds **3** (Mn, Ni and Co) show magnetic properties ranging from antiferromagnetic, to ferromagnetic and canted antiferromagnetic interactions.

Acknowledgements

Portions of the research were carried out at the light source DORIS III and PETRA III at DESY, a member of the Helmholtz Association (HGF). We thank Katrin Pflaum (DESY) for assistance at the beamline, Prof. Bensch (CAU Kiel), Henning Lühmann (CAU Kiel) and the Bensch group for the TG measurements and the DFG (STO-643/2 and WA 1116/17-2) for financial support.

Notes and references

1 M. T. Wharmby, S. R. Miller, J. A. Groves, I. Margiolaki, S. E. Ashbrook and P. A. Wright, *Dalton Trans.*, 2010, **39**, 6389–6391.
2 M. T. Wharmby, J. P. S. Mowat, S. P. Thompson and P. A. Wright, *J. Am. Chem. Soc.*, 2011, **133**, 1266–1269.
3 S. F. Tang, J. L. Song and J. G. Mao, *Eur. J. Inorg. Chem.*, 2006, 2011–2019; J.-G. Mao, *Coord. Chem. Rev.*, 2007, **251**, 1493–1520; A. Sonnauer, C. Nather, H. A. Hoppe, J. Senker and N. Stock, *Inorg. Chem.*, 2007, **46**, 9968–9974; Y. Zhu, Z. Sun, Y. Zhao, J. Zhang, X. Lu, N. Zhang, L. Liu and F. Tong, *New J. Chem.*, 2009, **33**, 119–124.
4 Y. Ji, X. Ma, X. Wu, N. Wang, Q. Wang and X. Zhou, *Catal. Lett.*, 2007, **118**, 187–194; X.-J. Zhang, T.-Y. Ma and Z.-Y. Yuan, *J. Mater. Chem.*, 2008, **18**, 2003–2010; M. Deng, Y. Ling, B. Xia, Z. Chen, Y. Zhou, X. Liu, B. Yue and H. He, *Chem.–Eur. J.*, 2011, **17**, 10323–10328; M. J. Beier, W. Kleist, M. T. Wharmby, R. Kissner, B. Kimmerle, P. A. Wright, J.-D. Grunwaldt and A. Baiker, *Chem.–Eur. J.*, 2012, **18**, 887–898; C. Queffélec, M. Petit, P. Janvier, D. A. Knight and B. Bujoli, *Chem. Rev.*, 2012, **112**, 3777–3807; K. J. Gagnon, H. P. Perry and A. Clearfield, *Chem. Rev.*, 2011, **112**, 1034–1054.

5 V. Chandrasekhar, P. Sasikumar, R. Boomishankar and G. Anantharamian, *Inorg. Chem.*, 2006, **45**, 3344–3351; Z. Y. Du, H. B. Xu and J. G. Mao, *Inorg. Chem.*, 2006, **45**, 9780–9788; D. Kong, J. Zon, J. McBee and A. Clearfield, *Inorg. Chem.*, 2006, **45**, 977–986; Z.-Y. Du, X.-L. Li, Q.-Y. Liu and J.-G. Mao, *Cryst. Growth Des.*, 2007, **7**, 1501–1507; Z.-Y. Du, A. V. Prosvirin and J.-G. Mao, *Inorg. Chem.*, 2007, **46**, 9884–9894.
6 A. Sonnauer, M. Feyand and N. Stock, *Cryst. Growth Des.*, 2009, **9**, 586–592.
7 M. Feyand, C. Nather, A. Rothkirch and N. Stock, *Inorg. Chem.*, 2010, **49**, 11158–11163.
8 M. Feyand, A. Hübner, A. Rothkirch, D. S. Wragg and N. Stock, *Inorg. Chem.*, 2012, **51**, 12540–12547.
9 R. C. Wang, Y. P. Zhang, H. L. Hu, R. R. Frausto and A. Clearfield, *Chem. Mater.*, 1992, **4**, 864–871; J. G. Mao, Z. K. Wang and A. Clearfield, *Inorg. Chem.*, 2002, **41**, 6106–6111; D. M. Poojary, B. L. Zhang and A. Clearfield, *J. Am. Chem. Soc.*, 1997, **119**, 12550–12559.
10 C. Schmidt, M. Feyand, A. Rothkirch and N. Stock, *J. Solid State Chem.*, 2012, **188**, 44–49.
11 Y.-F. Yang, Y.-S. Ma, S.-S. Bao and L.-M. Zheng, *Dalton Trans.*, 2007, 4222–4226.
12 A. Sonnauer and N. Stock, *J. Solid State Chem.*, 2008, **181**, 3065–3070.
13 K. J. Rao, B. Vaidhyanathan, M. Ganguli and P. A. Ramakrishnan, *Chem. Mater.*, 1999, **11**, 882–895.
14 S. Bauer and N. Stock, *Chem. Unserer Zeit*, 2007, **41**, 390–398.
15 N. Stock, *Microporous Mesoporous Mater.*, 2010, **129**, 287–295.
16 A. Sonnauer and N. Stock, *Eur. J. Inorg. Chem.*, 2008, **2008**, 5038–5045.
17 P. M. Forster, N. Stock and A. K. Cheetham, *Angew. Chem., Int. Ed.*, 2005, **44**, 7608–7611.
18 P. Maniam, C. Näther and N. Stock, *Eur. J. Inorg. Chem.*, 2010, **2010**, 3866–3874.
19 P. Maniam and N. Stock, *Inorg. Chem.*, 2011, **50**, 5085–5097; N. Reimer, B. Gil, B. Marszalek and N. Stock, *CrystEngComm*, 2012, **14**, 4119–4125.
20 F. Costantino, T. Bataille, N. Audebrand, E. Le Fur and C. Sangregorio, *Cryst. Growth Des.*, 2007, **7**, 1881–1888.
21 N. Stock, A. Stoll and T. Bein, *Microporous Mesoporous Mater.*, 2004, **69**, 65–69.
22 K. Moedritzer and R. R. Irani, *J. Org. Chem.*, 1966, **31**, 1603–1607.
23 T. Wroblewski, O. Clauß, H. A. Crostack, A. Ertel, F. Fandrich, C. Genzel, K. Hradil, W. Ternes and E. Woldt, *Nucl. Instrum. Methods Phys. Res., Sect. A*, 1999, **428**, 570–582.
24 O. H. Seeck, C. Deiter, K. Pflaum, F. Bertam, A. Beerlink, H. Franz, J. Horbach, H. Schulte-Schrepping, B. M. Murphy, M. Greve and O. Magnussen, *J. Synchrotron Radiat.*, 2012, **19**, 30–38.
25 Accelrys, *Materials Studio 5.5*, (2011).
26 J. Grehn and J. Krause, *Metzler Physik*, Schroedel Verlag, Hannover, 3rd edn, 1998.
27 E. Barsoukov and J. R. MacDonald, *Impedance spectroscopy*, Wiley & Sons, New Jersey, 2nd edn, 2005.
28 G. Alberti, M. Casciola, L. Massinelli and B. Bauer, *J. Membr. Sci.*, 2001, **185**, 73–81.
29 P. Rajiv, R. E. Dinnebier and M. Jansen, *Mater. Sci. Forum*, 2010, 97.
30 B.-P. Yang, A. V. Prosvirin, Y.-Q. Guo and J.-G. Mao, *Inorg. Chem.*, 2008, **47**, 1453–1459.
31 R. M. P. Colodrero, P. Olivera-Pastor, E. R. Losilla, D. Hernández-Alonso, M. A. G. Aranda, L. Leon-Reina, J. Rius, K. D. Demadis, B. Moreau, D. Villemin, M. Palomino, F. Rey and A. Cabeza, *Inorg. Chem.*, 2012, **51**, 7689–7698.
32 R. Marschall, J. Rathouský and M. Wark, *Chem. Mater.*, 2007, **19**, 6401–6407.
33 L. Carrette, K. A. Friedrich and U. Stimming, *Fuel Cells*, 2001, **1**, 5–39; M. N. T. A. Zawodzinsky, L. O. Sillerud and S. Gottesfeld, *J. Phys. Chem.*, 1991, **95**, 6040–6044.
34 C. Laberty-Robert, K. Valle, F. Pereira and C. Sanchez, *Chem. Soc. Rev.*, 2011, **40**, 961–1005; P. Tolle, C. Kohler, R. Marschall, M. Sharifi, M. Wark and T. Frauenheim, *Chem. Soc. Rev.*, 2012, **41**, 5143–5159.

